Electric dipole spin resonance of two-dimensional semiconductor spin qubits

Matthew Brooks[*] and Guido Burkard
Department of Physics, University of Konstanz, D-78464 Konstanz, Germany

Monolayer transition metal dichalcogenides (TMDs) offer a novel two-dimensional platform for semiconductor devices. One such application, whereby the added low-dimensional crystal physics (i.e., optical spin selection rules) may prove TMDs a competitive candidate, are quantum dots as qubits. The band structure of TMD monolayers offers a number of different degrees of freedom and combinations thereof as potential qubit bases, primarily electron spin, valley isospin, and the combination of the two due to the strong spin-orbit coupling known as a Kramers qubit. Pure spin qubits in monolayer MoX_2 (where $X = $ S or Se) can be achieved by energetically isolating a single valley and tuning to a spin degenerate regime within that valley by a combination of a sufficiently small quantum dot radius and a large perpendicular magnetic field. Within such a TMD spin qubit, we theoretically analyze single-qubit rotations induced by electric dipole spin resonance. We employ a rotating-wave approximation within a second-order time-dependent Schrieffer-Wolf effective Hamiltonian to derive analytic expressions for the Rabi frequency of single-qubit oscillations, and optimize the mechanism or the parameters to show oscillations up to 250 MHz. This is significantly faster than similar predictions found for TMD qubits in the Kramers pair spin-valley or valley-only basis as well as experimental results for conventional semiconductor devices.

I. INTRODUCTION

Transition metal dichalcogenides (TMDs) are graphitelike indirect band-gap semiconductors in bulk, that when isolated down to the monolayer (ML) limit become two-dimensional visible range direct band-gap semiconductors, with a hexagonal crystal lattice structure [1–7]. The combination of optically addressable electron spin and valley isospin degrees of freedom [8,9] and strong spin-orbit coupling [10,11] within a mechanically flexible ML [12,13] which may be stacked with other ML materials as part of the van der Waals (vdW) heterostructure engineering architecture [14–16], has allowed for TMDs to be a viable and desirable host for quantum technologies. Quantum dots (QDs) [17], single-photon emitters [13,18,19], gate-defined nanowires [20,21], topological materials [22,23], ML superconductors [24,25], as well as spin- [26,27] and valleytronics [28,29] have all been proposed or demonstrated with TMD MLs.

Chemically, the semiconducting TMD MLs consist of MX_2 where $M = $ Mo or W and $X = $ S or Se, where the M atomic layer is sandwiched between two X atomic layers [1–4], with broken inversion symmetry [1,9,30], and an M-X alternating hexagonal structure in the plane of the ML [1,3,31]. The M atoms introduce strong spin-orbit coupling [10,11], which with the broken inversion symmetry gives rise to spin-split conduction and valence bands [8,32,33]. Under an out-of-plane magnetic field, the splitting between the spin states in the conduction band is shifted due to both a spin- and valley-Zeeman effect [34–37] introduced by a significant Berry curvature at the band edges [34,38,39]. Additionally, the Berry curvature allows for optically addressable spin-valley states by correctly applied circularly polarized light [8,38].

QDs in TMD monolayers have been demonstrated by a number of different methods. Electrostatic gating [17], strain [13,18], nanoflakes [40,41], and lattice defects [42] have all been shown to achieve zero-dimensional behavior in TMD monolayers. Strain and electrostatic gating, however, exhibit the most promise for QDs for quantum information purposes [43], and a number of different methods of implementing a qubit in a TMD QD have been proposed including spin-valley Kramers qubits [41,44], in which one- and two-qubit gates have been proposed [44,45], valley qubits [40,41], and pure-spin qubits [46]. Pure-spin qubits were shown to be achievable by tuning a combination of the QD radius and the out-of-plane magnetic field such that, within one valley, a near spin degeneracy is reached. The magnetic field required to do so in specifically an MoS$_2$ QD is high ($\sim$20–30 T) when considering only the natural spin- and valley-Zeeman contributions of the ML, even though this ML contains the smallest energy to overcome. However, as previously mentioned, one of the benefits of 2D semiconductors is the access to vdW heterostructure engineering. Thus, it has been shown that by layering TMDs with magnetic monolayers such as CrI$_3$, EuS, and EuO, local time reversal symmetry violation in the TMD occurs, significantly enhancing the valley-Zeeman effect observed in the TMD [16,47–52]. A similar result may also be achieved with doping [53]. The modularity of vdW heterostructure devices, along with an optically initializable spin state, makes TMD QDs a strong contender to more conventional bulk semiconductor qubit realizations.

Towards building a 2D quantum processor, the next step, after realizing a qubit, is a scheme for single-qubit gates,

*matthew.brooks@uni-konstanz.de

i.e., a reliable method of single-qubit state initialization and control. In this paper, we demonstrate that electric dipole spin resonance (EDSR) may be achieved in TMD pure-spin qubits. EDSR requires the coupling of the qubit spin states to an external ac-electric field [54,55], which drives rotations between the spin states, such that ideally microwave pulses can be used to perform the desired single-qubit gate. This has been theoretically shown to be achievable in TMD QDs adopting a Kramers qubit architecture, with the aid of an additional lattice defect to mix the valley states [44]. We show that in a valley-polarized pure-spin qubit architecture, EDSR is achievable and with some parameter optimization (dot radius, magnetic fields, etc.) oscillations of the qubit in the ∼100 MHz regime are feasible.

This paper is structured as follows: First, in Sec. II, the TMD QD Hamiltonian is given and the studied material type and parameter regime for the pure-spin qubit architectures is detailed. Then, in Sec. III, the EDSR mechanism is introduced in detail, giving all relevant matrix elements, as well as an effective qubit Hamiltonian given by a time-dependent Schrieffer-Wolff transformation. Third, in Sec. IV, the rotating-wave approximation (RWA) is applied to derive expressions for the Rabi frequency in the rotating frame. This is followed in Sec. V by an analysis of the relevant parameters of the system to maximize the qubit frequency. Lastly, in Sec. VI, a discussion and comparison of this architecture with other known architectures is provided.

II. MONOLAYER TMD QUANTUM DOTS

In this paper, we assume an electrostatic-gate-defined QD in a TMD monolayer, as is schematically shown in the inset of Fig. 1. With the appropriate selection of the TMD type, and a sufficiently large external magnetic field, it has been shown that the spin-valley locking may be overcome to provide a host for a valley-polarized pure-spin qubit [46].

A. Effective Hamiltonian

The energy levels of a single electron in a TMD quantum dot in a perpendicular magnetic field ($B_\perp$) at the K or K' valleys may be obtained by solving the effective low-energy Hamiltonian [43,46]

$$H_{B_\perp}^{\tau,s} = \hbar\omega_c^{\tau,s}\alpha_+\alpha_- + \tau s\frac{\Delta_{\mathrm{cb}}}{2} + \frac{1+\tau}{2}\frac{B_\perp}{|B_\perp|}\hbar\omega_c^{\tau,s}$$
$$+ \frac{1}{2}(\tau g_{\mathrm{vl}} + s g_{\mathrm{sp}})\mu_B B_\perp, \tag{1}$$

where $\tau = \pm 1$ is the valley index with $1(-1) \equiv K(K')$, $s = \pm 1$ is the spin index with $1(-1) \equiv \uparrow(\downarrow)$, $\omega_c^{\tau,s}$ is the spin-valley-dependent cyclotron frequency, Δ_{cb} is the spin-orbit splitting in the conduction band of the TMD, g_{vl} and g_{sp} are the valley and spin out-of-plane g-factors, respectively, and μ_B is the Bohr magneton. The spin-valley dependence of $\omega_c^{\tau,s}$ is due to the spin-valley dependence of the effective mass at the band edges given as $1/m_{\mathrm{eff}}^{\tau,s} = 1/m_0 - \tau s/\delta m_{\mathrm{eff}}$, where δm_{eff} is contingent on the TMD type and m_0 is the free-electron mass. The modified wave-number operators $\alpha_\pm$ are $\alpha_\pm = \mp i l_B q_\pm/\sqrt{2}$ where $l_B = \sqrt{\hbar/eB_\perp}$ is the magnetic length and $q_\pm = q_x \pm iq_y$ where $q_k = -i\partial_k$. The potential of
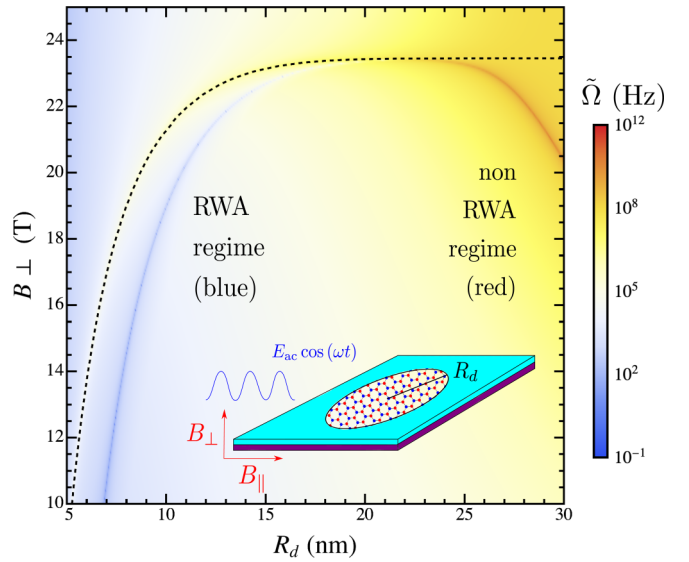

FIG. 1. Rabi frequency $\tilde{\Omega}$ of a MoS$_2$ QD in dependence of the dot radius R_{d} and out-of-plane magnetic field $B_\perp$ where $E_{\mathrm{ac}} = 10^{-2}$ mV/nm and $B_\parallel = 1$ T. The black dashed line gives the points of spin degeneracy in the ground states of the K' valley. Note that the region where the RWA is valid is where the frequencies calculated off-resonantly from the spin degeneracy line are small (blue), while the region where the maximum $\tilde{\Omega}$ deviates from the spin degeneracy line is where the RWA breaks down. Inset: Diagram of the setup considered in this paper of a gated TMD QD of radius R_{d} (purple representing the TMD ML and cyan representing the top gate), exposed to a static out-of-plane magnetic field $B_\perp$, in-plane magnetic field $B_\parallel$, and an in-plane ac-electric field E_{ac}.

the QD is assumed to be an infinite square well of radius R_{d}, which is reasonable when assuming the electrostatic gates of the dot to be contacted to or separated by one to two layers of 2D dielectric hexagonal boron nitride [17,56]. Thus the quantum dot levels as a function of $B_\perp$ and R_{d} are given as

$$\tilde{\varepsilon}_{n,l}^{\tau,s} = \varepsilon_{n,l}^{\tau,s} + \tau s\frac{\Delta_{\mathrm{cb}}}{2}, \tag{2}$$

where

$$\varepsilon_{n,l}^{\tau,s} = \hbar\omega_c^{\tau,s}\left(\frac{1+\tau}{2}\frac{B_\perp}{|B_\perp|} + \frac{|l|+l}{2} - \gamma_{n,l}\right)$$
$$+ \frac{1}{2}(\tau g_{\mathrm{vl}} + s g_{\mathrm{sp}})\mu_B B_\perp. \tag{3}$$

Here, $\gamma_{n,l}$ is the nth solution to $M(\gamma_{n,l}, |l|+1, R_{\mathrm{d}}^2/2l_B^2) = 0$, where $M(a, b, c)$ is the confluent hypergeometric function of the first kind, given by the hard-wall boundary condition to Eq. (1).

B. Single-dot spin qubit

The spin-valley locking due to spin-orbit coupling and crystal symmetries can be shown to be overcome, resulting in a pure-spin qubit [46] with a TMD QD as opposed to a spin-valley Kramers' qubit [44]. By selecting the appropriate TMD type, dot size, and perpendicular magnetic field, a regime where $\varepsilon_{n,l}^{K(K'),\uparrow} = \varepsilon_{n,l}^{K(K'),\downarrow}$ may be achieved. MoS$_2$ is
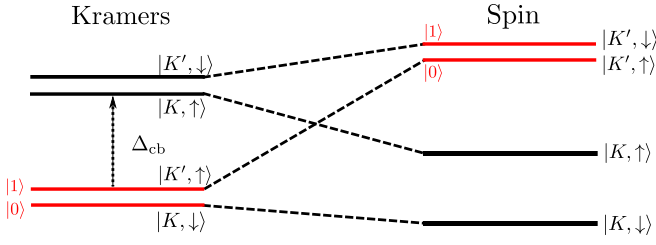
FIG. 2. Level diagrams of the orbital ground states for all combinations of spin and valley of an MoX$_2$ QD operating in a Kramers qubit basis (small external out-of-plane magnetic field $B_\perp$) and a spin qubit basis (large external out-of-plane magnetic field $B_\perp$). The levels in which the qubits are encoded are shown in red.

the semiconducting TMD monolayer with the smallest zero-field spin splitting in the conduction band Δ_{cb} and a δm_{eff} such that the condition $\varepsilon_{1,0}^{K',\uparrow} = \varepsilon_{1,0}^{K',\downarrow}$ may be achieved for $B_\perp \approx 16$ T in the first excited state ($n = 1, l = -1$) and $B_\perp \approx 21$ T in the ground state ($n = 1, l = 0$) assuming $R_d \approx 10$ nm. This is shown with comparison to a Kramers qubit in Fig. 2. Assuming that the QD is charged by a valley-polarized source, either optically or by valley-polarized leads, a pure-spin qubit in an MoS$_2$ monolayer gated quantum dot may be realized.

III. ELECTRIC DIPOLE SPIN RESONANCE

A. External influences

To achieve control over the qubit spin states, two additional ingredients to the spin-orbit interaction inherent in the crystal are needed: a spin-mixing interaction and a driving field. These are achieved by subjecting the QD to a static in-plane magnetic field and ac in-plane electric field.

The Hamiltonian describing an in-plane magnetic field along the x direction is given as

$$H_{B_\parallel} = \tfrac{1}{2}\mu_B g_\parallel B_\parallel s_x, \tag{4}$$

where $g_\parallel$ is the in-plane g-factor, $B_\parallel$ is the in-plane magnetic field, and s_i where $i = (x, y, z)$ is the ith spin Pauli matrix, i.e., $s_i = (\hbar/2)\sigma_i$. The in-plane g-factor $g_\parallel$ is assumed in this paper to originate purely from the spin degree of freedom, and thereby to be equal to $g_\parallel = 2$. The out-of-plane g-factor g_s is material dependent and given by the same seven-band $k \cdot p$ analysis used to derive the effective Hamiltonian Eq. (1) [43].

The real-space Hamiltonian of an ac-electric driving field along the x direction is given as

$$\tilde{H}_{\mathrm{ac}} = e\hat{x}E_{\mathrm{ac}}\cos(\omega t), \tag{5}$$

where e is the elementary charge, E_{ac} and ω denote the field strength and frequency of the ac field, and t is time. In the orbital basis this can be rewritten as approximately (see Appendix A)

$$H_{\mathrm{ac}} = \frac{eE_{\mathrm{ac}}R_d \cos(\omega t)}{2\sqrt{2}}\sigma_x, \tag{6}$$

where σ_i is the ith orbital Pauli matrix. From these matrix elements, the full Hamiltonian for ESDR in TMD QDs may be written.

B. 4 × 4 valley-polarized Hamiltonian

Due to our choice of material and $B_\perp$ direction (positive along the z axis), the valley in which the spin qubit is achieved is the K' (see Fig. 2). From all the elements collected in Secs. II and III A, the full Hamiltonian of the valley-polarized TMD dot with an in-plane magnetic field and ac-electric field is

$$H_{K'} = \frac{1}{2}\begin{pmatrix} 2\varepsilon_{1,0}^{K',\uparrow} - \Delta_{\mathrm{cb}} & \mu_B g_\parallel B_\parallel & \frac{eE_{\mathrm{ac}}R_d \cos(\omega t)}{\sqrt{2}} & 0 \\ \mu_B g_\parallel B_\parallel & 2\varepsilon_{1,0}^{K',\downarrow} + \Delta_{\mathrm{cb}} & 0 & \frac{eE_{\mathrm{ac}}R_d \cos(\omega t)}{\sqrt{2}} \\ \frac{eE_{\mathrm{ac}}R_d \cos(\omega t)}{\sqrt{2}} & 0 & 2\varepsilon_{1,-1}^{K',\uparrow} - \Delta_{\mathrm{cb}} & \mu_B g_\parallel B_\parallel \\ 0 & \frac{eE_{\mathrm{ac}}R_d \cos(\omega t)}{\sqrt{2}} & \mu_B g_\parallel B_\parallel & 2\varepsilon_{1,-1}^{K',\downarrow} + \Delta_{\mathrm{cb}} \end{pmatrix} \tag{7}$$

for the qubit basis and the first excited orbital spin states ($\{|l = 0, K', \uparrow\rangle, |l = 0, K', \downarrow\rangle, |l = -1, K', \uparrow\rangle, |l = -1, K', \downarrow\rangle\}$) to which the qubit couples by the driving field. From this, an approximate 2 × 2 time-dependent qubit Hamiltonian may be derived.

C. Time-dependent Schrieffer-Wolff transformation

A second-order time-dependent Schrieffer-Wolff transformation (TDSWT) is employed to isolate a time-dependent effective qubit Hamiltonian [57] (for a complete derivation, see Appendix B). The relevant terms of the transformation are

$$H_{\mathrm{EDSR}}(t) = \tilde{\mathcal{H}}^{(0)} + \tilde{\mathcal{H}}^{(1)} + \tilde{\mathcal{H}}^{(2)}(t), \tag{8}$$

where

$$\tilde{\mathcal{H}}^{(0)} = \sum_{s,l} \varepsilon_{1,l}^{\tilde{\tau},s} |s, l\rangle \langle s, l|, \tag{9a}$$

$$\tilde{\mathcal{H}}^{(1)} = \frac{\mu_B g_\parallel B_\parallel}{2} s_x, \tag{9b}$$

$$\tilde{\mathcal{H}}(t)^{(2)} = \frac{E_{\mathrm{ac}}^2 R_d^2 [1 + \cos(2\omega t)]}{36\hbar\omega_{s,s}^{0,-1}}\sigma_z, \tag{9c}$$

where $\omega_{s,s'}^{l,l'}$ is the energy difference between the two QD levels $\varepsilon_{1,l}^{K',s}$ and $\varepsilon_{1,l'}^{K',s'}$ expressed as an angular frequency such that, for example, $\varepsilon_{1,0}^{K',\uparrow} - \varepsilon_{1,-1}^{K',\downarrow} = \hbar\omega_{\uparrow,\downarrow}^{0,-1}$. To ensure the validity of our perturbative TDSWT analysis, the off-diagonal matrix elements of the Hamiltonian need to be significantly smaller than its on-diagonal matrix elements.

Therefore, the corresponding small parameters are the electric field strength $eE_{ac}R_d/\hbar\omega_{\uparrow,\downarrow}^{0,0} \ll 1$ and in-plane magnetic field strength $\mu_B g_\parallel B_\parallel/2\hbar\omega_{\uparrow,\downarrow}^{0,0} \ll 1$. Accordingly, Eq. (8)

leads to a block diagonal Hamiltonian for which the relevant time-dependent qubit basis portion may be extracted as

$$H_{EDSR}(t) = \begin{pmatrix} \varepsilon_{1,0}^{K',\uparrow} + \frac{e^2 E_{ac}^2 R_d^2 [1+\cos(2\omega t)]}{16\hbar\omega_{\uparrow,\uparrow}^{0,-1}} & \frac{\mu_B g_\parallel B_\parallel}{2} \\ \frac{\mu_B g_\parallel B_\parallel}{2} & \varepsilon_{1,0}^{K',\downarrow} + \frac{e^2 E_{ac}^2 R_d^2 [1+\cos(2\omega t)]}{16\hbar\omega_{\downarrow,\downarrow}^{0,-1}} \end{pmatrix}. \tag{10}$$

IV. RABI OSCILLATIONS

From the time-dependent qubit Hamiltonian given in Eq. (10), a transformation into the rotating basis may be performed and the rotating-wave approximation applied to derive the Rabi-oscillation frequency in the rotating frame as

$$\tilde{\Omega} = \frac{3\mu_B g_\parallel B_\parallel e^2 E_{ac}^2 R_d^2 \left(\omega_{\downarrow,\downarrow}^{0,-1} - \omega_{\uparrow,\uparrow}^{0,-1}\right)}{4\sqrt{\left(36\mu_B g_\parallel B_\parallel \omega_{\uparrow,\uparrow}^{0,-1} \omega_{\downarrow,\downarrow}^{0,-1} \hbar\right)^2 + \left(e^2 E_{ac}^2 R_d^2 [\omega_{\downarrow,\downarrow}^{0,-1} - \omega_{\uparrow,\uparrow}^{0,-1}] - 36\omega_{\uparrow,\downarrow}^{0,0} \omega_{\uparrow,\uparrow}^{0,-1} \omega_{\downarrow,\downarrow}^{0,-1} \hbar^2\right)^2}}. \tag{11}$$

Note that in this form, the implicit dependence of the Rabi frequency $\tilde{\Omega}$ on $B_\perp$ is within all the $\omega_{s,s'}^{l,l'}(B_\perp)$ frequencies while the dependence of $\tilde{\Omega}$ on the spin-orbit splitting of the conduction band Δ_{cb} is within $\omega_{\uparrow,\uparrow}^{0,-1}(B_\perp, \Delta_{cb})$ and $\omega_{\downarrow,\downarrow}^{0,-1}(B_\perp, \Delta_{cb})$. The difference between the two, however, present in the numerator of Eq. (11), is not dependent on the spin-orbit splitting. Note that, as the spin splitting due to the spin-orbit interaction is decreased, so too is the maximum Rabi frequency achievable, and as $\Delta_{cb} \to 0$ the in-plane magnetic field small parameter condition of the TDSWT is violated and all of the calculations made up to this point are no longer valid.

A further simplification of Eq. (11) may be given as its dominant term,

$$\Omega = \frac{\mu_B g_\parallel B_\parallel e^2 E_{ac}^2 R_d^2 \left(\varepsilon_{1,-1}^{K',\uparrow} - \varepsilon_{1,-1}^{K',\downarrow}\right)}{48\Delta_{cb} \left[\varepsilon_{1,0}^{K',\uparrow} - \varepsilon_{1,-1}^{K',\uparrow}\right]\left[\varepsilon_{1,0}^{K',\downarrow} - \varepsilon_{1,-1}^{K',\downarrow}\right]\hbar^2}, \tag{12}$$

assuming $\varepsilon_{1,0}^{K',\uparrow} \approx \varepsilon_{1,0}^{K',\downarrow}$, i.e., operating at the spin qubit regime. The physics of the terms dropped from (11) to give (12) are apparent from the following expansion,

$$\tilde{\Omega} = \Omega(1 + \delta_1 + \delta_2 + \cdots), \tag{13}$$

where

$$\delta_1 = \frac{e^2 E_{ac}^2 R_d^2 \left[\omega_{\downarrow,\downarrow}^{0,-1} - \omega_{\uparrow,\uparrow}^{0,-1}\right]}{36\omega_{\uparrow,\downarrow}^{0,0} \omega_{\uparrow,\uparrow}^{0,-1} \omega_{\downarrow,\downarrow}^{0,-1} \hbar^2}$$
$$\times \left(1 + \frac{e^2 E_{ac}^2 R_d^2 \left[\omega_{\downarrow,\downarrow}^{0,-1} - \omega_{\uparrow,\uparrow}^{0,-1}\right]}{72\omega_{\uparrow,\uparrow}^{0,0} \omega_{\uparrow,\uparrow}^{0,-1} \omega_{\downarrow,\downarrow}^{0,-1} \hbar^2}\right), \tag{14a}$$

$$\delta_2 = \frac{(\mu_B g_\parallel B_\parallel)^2}{2(\omega_{\uparrow,\downarrow}^{0,0}\hbar)^2}. \tag{14b}$$

From this, δ_1 can be reasoned as a shift due to the ac Stark effect as it is a perturbation in a higher order of E_{ac} and δ_2 is the plane Zeeman shift due to $B_\parallel$. From this form of the Rabi frequency, the effect of the EDSR fields may be probed.

First, the effect of the strength of the ac-electric field E_{ac} is clearly quadratic. As such, this value shall be fixed at 10^{-2} mV/nm to allow for a direct comparison with previous proposals concerning Kramers qubits [44]. This is an achievable electric field amplitude that is consistent the small parameter conditions stated in Sec. III C. The effect of $B_\perp$ can be seen in both Figs. 3 and 4. Figure 3 shows the dependence of Ω on $B_\perp$ for a number of dot radii. There is a clear peak for each radius and clear minimum, where $\Omega \to 0$, at which $\omega_{\downarrow,\downarrow}^{0,-1} = \omega_{\uparrow,\uparrow}^{0,-1}$. The reason for this interference is clear in Fig. 4. The avoided crossings for the qubit states and the orbitally excited states do not align with $B_\perp$, and as such, there are values of $B_\perp$ that are after one avoided crossing and before the second. This manifests itself in Fig. 4 where each of the kinks in the gradient of the $\omega_{\downarrow,\downarrow}^{0,-1}$ and $\omega_{\uparrow,\uparrow}^{0,-1}$ lines occur at the avoided crossings. It is in between these two kinks that the destructive interference is such that $\omega_{\downarrow,\downarrow}^{0,-1} = \omega_{\uparrow,\uparrow}^{0,-1}$
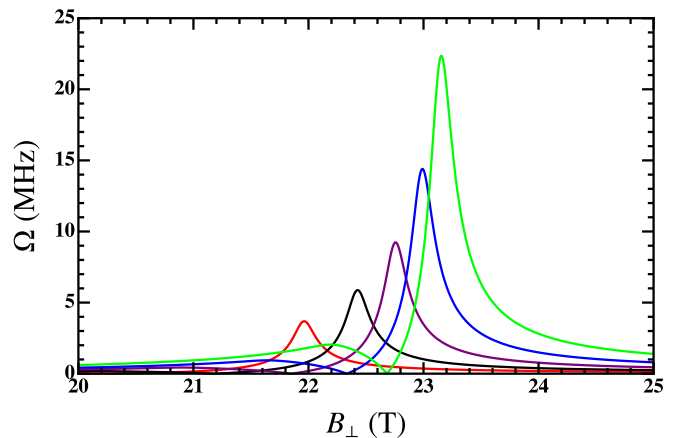

FIG. 3. The out-of-plane magnetic field $B_\perp$ dependence of the Rabi frequency Ω for MoS$_2$ QDs with $R_d = 11$ nm (red), 12 nm (black), 13 nm (purple), 14 nm (blue), and 15 nm (green), with $E_{ac} = 10^{-2}$ mV/nm and $B_\parallel = 50$ mT.
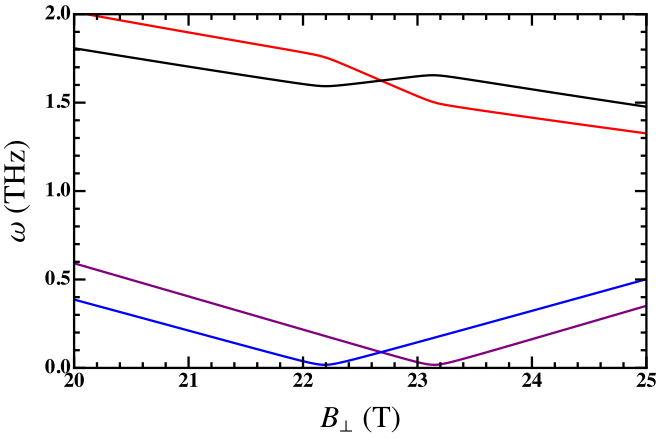
FIG. 4. The out-of-plane magnetic field $B_\perp$ dependence of the QD level splittings expressed as angular frequencies $\omega_{\downarrow,\downarrow}^{0,-1}$ (red), $\omega_{\uparrow,\uparrow}^{0,-1}$ (black), $\omega_{\uparrow,\downarrow}^{0,0}$ (purple), and $\omega_{\uparrow,\downarrow}^{-1,-1}$ (blue), for MoS$_2$ QDs of with $E_{ac} = 10^{-2}$ mV/nm, $B_\parallel = 50$ mT, and $R_d = 15$ nm.

and $\Omega \to 0$. The effect of $B_\parallel$ is also not fully apparent from Eq. (12). Of course, from the numerator as $B_\parallel \to 0$ so does $\Omega \to 0$, as there is no spin mixing mechanism at this limit, but the relationship between the two is not linear, as a wider avoided crossing can be detrimental to the rotation speed. As is seen in Fig. 5, there is a clear peak in the achievable Ω at some small $B_\parallel$ specific and inversely proportional to the dot radius. For values of $B_\parallel$ larger than this critical field strength, the potential Rabi frequency decreases, converging to some minimum frequency that is proportional to the dot radius.

V. OPTIMAL OPERATIONS

Understanding in detail the effects of each of the contributing EDSR mechanisms on the derived single-qubit rotational frequency now allows for an optimization of the EDSR procedure. However, there is still one parameter with which the mechanism may be optimized, the dot radius. Figure 1 gives
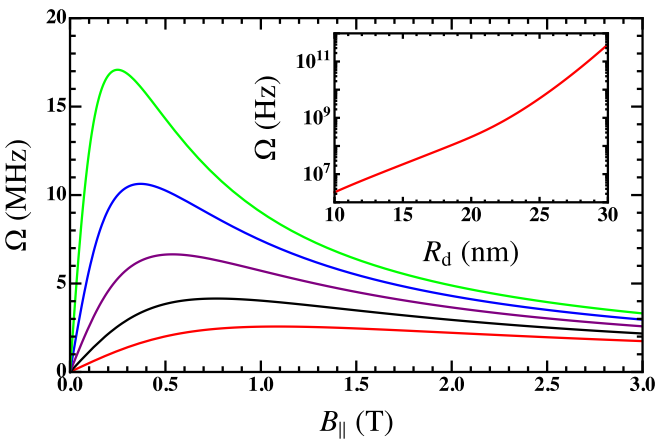

FIG. 5. Rabi frequency on resonance for MoS$_2$ QDs with $R_d = 11$ nm (red), 12 nm (black), 13 nm (purple), 14 nm (blue), and 15 nm (green), and $E_{ac} = 10^{-2}$ mV/nm. Inset: Extracted maximum Rabi frequency Ω with dot radius R_d for MoS$_2$ QDs with $E_{ac} = 10^{-2}$ mV/nm and $B_\parallel = 1$ T.
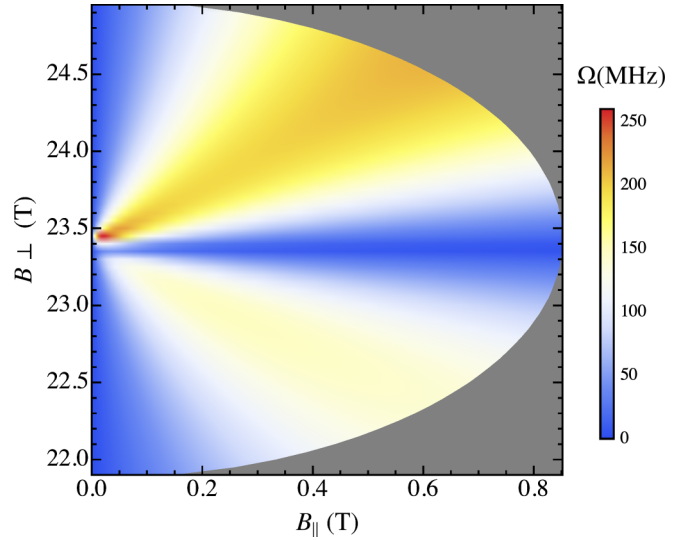

FIG. 6. The out-of-plane $B_\perp$ and in-plane $B_\parallel$ magnetic field dependencies of the Rabi frequency Ω for an MoS$_2$ QD of radius $R_d = 20$ nm where $E_{ac} = 10^{-2}$ mV/nm only within the microwave qubit detuning range.

$\tilde{\Omega}$ in dependence of R_d and $B_\perp$ at constant E_{ac} and $B_\parallel$, showing a clear peak running along the spin degeneracy line as well as the interference line under the peak. Note that here the full expression $\tilde{\Omega}$ is plotted as to demonstrate where the RWA starts to break down, as for $R_d \gtrsim 22.5$ nm, the higher-order terms deviate the peak from around the spin degeneracy point and the Rabi frequency diverges past the reasonable range of the assumed driving frequency (microwave). The reduced form of the Rabi frequency Ω gives exactly the same result below this point, without showing the deviation at larger dot radii. The inset of Fig. 5 shows more explicitly the R_d dependence of the maximum Rabi frequency achievable when at a fixed $B_\parallel = 1$ T. Here, a close-to-exponential increase in achievable Rabi frequency is observed. This trend is easily exploitable but comes with a significant cost in $B_\perp$ needed to achieve spin qubits with increasing dot radius.

As a proposal for an optimal operational regime, consider a dot of $R_d = 20$ nm. To satisfy both the conditions of the RWA and experimental preferences, only the regime where the qubit detuning is within the microwave range <300 GHz shall be considered. This is shown in Fig. 6, where a clear peak region at $B_\perp = 23.5$ T and $B_\parallel = 20$ mT can be seen. At this optimized point a very desirable Rabi frequency of ~ 250 MHz is reached. However, there is a band where Rabi frequencies ~ 100 MHz are attainable, allowing for less precise control of the magnetic fields to access a desirable frequency range.

VI. DISCUSSION

To implement a pure-spin qubit with fast single-gate operations we find that a good choice consists of an MoS$_2$ QD of radius $R_d = 20$ nm, in a external out-of-plane magnetic field $B_\perp = 23.5$ T, in-plane magnetic field $B_\parallel = 20$ mT, and a microwave frequency ac-electric field of strength $E_{ac} = 10^{-2}$ mV/nm. This allows for a Rabi frequency of $\Omega = 250$ MHz. All of the assumed field parameters are within

reasonable viability. The $B_\perp$ requirement is high, however, this can be reasonably mitigated by vdW heterostructure engineering with magnetic monolayers. All calculations given assume the qubit is implemented in a free-standing TMD ML, to give an upper limit on what would be experimentally required. Recent advances in vdW heterostructure engineering have shown that significant valley-Zeeman enhancement can be achieved by layering the TMD on a ML or low-dimensional magnetic material [16,47,48]. Ideally, a vdW stack of hexagonal boron nitride (hBN)-CrI$_3$ or EuS-MoS$_2$-hBN would be used to implement a TMD spin quantum processor. The purpose of the hBN is to protect the other MLs from degradation as well as improve the optical response of the TMD for state initialization [58–60].

The gate speed shown here is an order of magnitude faster within reasonable experimental limitations than has been shown in the alternative single-dot approach to TMD qubits, the Kramers qubit [44]. This assumes a clean crystal, unlike the Kramers qubit that requires a defect to mix the valleys. While defects are currently inherent to TMD samples, they are usually undesirable, and in the proposed pure-spin qubit scheme offer a dephasing mechanism. However, the K-valley levels are higher in energy and become more energetically separated at lower R_d, therefore, some tradeoff between gate speed and stability can be made in the case of valley-mixing crystal defects. Additionally, there has been recent significant progress in synthesizing low defect rate monolayers by chemical as opposed to mechanical means [61].

The ∼100-MHz single-gate rotations makes this 2D qubit implementation competitive with more conventional bulk semiconductor architectures due to the intrinsic spin-orbit coupling, removing the need for spin-mixing micromagnets [62] of the MLs and the validity of a square walled potential of the dot model due to gating directly to an ML or ML-hBN heterostructure [46]. Both GaAs and Si 2D electron gas gated single spin qubits have experimentally shown Rabi oscillations in the order of ∼10 MHz [54,63,64]. However, in TMDs, these fast gate speeds are required as spin lifetimes have only been measured up to a few nanoseconds [65]. This is, however, expected to improve with the advent of cleaner crystal samples. The promise of similar to improved speeds attainable with the TMD device proposed here, in a flexible and optically active medium, further position 2D semiconductors as exciting novel materials for quantum device applications.

APPENDIX A: DIPOLE MATRIX

The dipole matrix elements represent the off-diagonal elements that in the case of this paper couple the qubit states with the first excited orbital states. These are calculated as follows,

$$d_{nl,n'l'} = \langle \psi_{nl} | \tilde{H}_{ac} | \psi_{n'l'} \rangle, \quad (A1)$$

where $\tilde{H}_{ac}$ is given by (5). Here, the wave functions are derived from Eq. (1) as [46]

$$\psi_{n,l} = \mathcal{A}(\gamma_{n,l}, \rho) e^{il\theta} \rho^{|l|/2} e^{-\rho/2} M(\gamma_{n,l}, |l|+1, \rho), \quad (A2)$$

where $\mathcal{A}(\gamma_{n,l}, \rho)$ is the normalizing factor. Importantly for this paper, the matrix element $\langle \psi_{n,l} | \tilde{H}_{ac} | \psi_{n,l} \rangle = 0$ while $\langle \psi_{n,l} | \tilde{H}_{ac} | \psi_{n,l'} \rangle \neq 0$ for $l \neq l'$. The value of these matrix elements can be calculated numerically. The corresponding matrix element is dependent on $B_\perp$ and R_d, however, we find that the dependence on $B_\perp$ is so slight ($<0.01\%$) that for this paper we shall simply assume

$$\langle \psi_{0,1} | \tilde{H}_{ac} | \psi_{0,0} \rangle \approx \frac{eE_{ac}R_d}{2\sqrt{2}}. \quad (A3)$$

APPENDIX B: FULL TDSWT DERIVATION

The time-dependent Schrieffer-Wolff transformation is a perturbative method to derive an effective block diagonal Hamiltonian $\tilde{\mathcal{H}}(t)$ from a dense Hamiltonian $\mathcal{H}(t)$ such as Eq. (7) [57]. We proceed by applying the unitary transformation $U(t) = e^{-S(t)}$, such that

$$\tilde{\psi}(t) = e^{-S(t)} \psi(t), \quad (B1)$$

and, using the time-dependent Schrödinger equation, $-i\hbar \frac{\partial}{\partial t} \psi(t) + \mathcal{H}(t)\psi(t) = 0$, leading to the transformed Hamiltonian

$$\tilde{\mathcal{H}}(t) = e^{-S(t)} \mathcal{H}(t) e^{S(t)} + i\hbar \frac{\partial e^{-S(t)}}{\partial t} e^{S(t)}. \quad (B2)$$

Here, $S(t)$ is some block off-diagonal matrix. From this setup, a power-series expansion can then be applied which can be simplified to give

$$\tilde{\mathcal{H}}(t) = \sum_{j=0}^{\infty} \frac{1}{j!} [\mathcal{H}(t), S(t)]^{(j)} - i\hbar \sum_{j=0}^{\infty} \frac{1}{(j+1)!} [\dot{S}(t), S(t)]^{(j)}, \quad (B3)$$

where $[A,B]^{(0)} = A$ and $[A,B]^{(n+1)} = [[A,B]^{(n)}, B]$. Here, $S(t)$ is solved for by assuming $\tilde{\mathcal{H}}(t)_{\text{off-diagonal}} = 0$. At this point no approximation has been made. The approximation made to solve Eq. (B2) such that $\tilde{\mathcal{H}}(t)_{\text{off-diagonal}} = 0$ is a power-series expansion of the small parameters (in-plane electric and magnetic fields) of the $S(t)$ matrix,

$$S(t) = S(t)^{(1)} + S(t)^{(2)} + S(t)^{(3)} + \cdots, \quad (B4)$$

where $S(t)_n$ is the nth order of the power series.

At this point, all the necessary definitions have been made to perform a general TDSWT, and as such, now only a second-order perturbation of Eq. (7) will be considered with the small parameters being the electric field strength $eE_{ac}R_d/\hbar\omega_{\uparrow,\downarrow}^{0,0}(B_\perp) \ll 1$ and in-plane magnetic field strength $\mu_B g_\parallel B_\parallel/\hbar\omega_{\uparrow,\downarrow}^{0,0}(B_\perp) \ll 1$. The effective Hamiltonian with corrections up to second order is given by

$$\tilde{\mathcal{H}}(t) = \tilde{\mathcal{H}}^{(0)} + \tilde{\mathcal{H}}^{(1)} + \tilde{\mathcal{H}}(t)^{(2)}. \quad (B5)$$

From this, the expansions in $\tilde{\mathcal{H}}(t)$ can be solved from Eq. (B2) as

$$\tilde{\mathcal{H}}^{(0)} = \mathcal{H}_0, \quad (B6a)$$

$$\tilde{\mathcal{H}}^{(1)} = \mathcal{H}_1, \quad (B6b)$$

$$\tilde{\mathcal{H}}^{(2)}(t) = \tfrac{1}{2}[\mathcal{H}_2(t), S(t)^{(1)}]. \tag{B6c}$$

Here, $\mathcal{H}_0$ is the diagonal part of Eq. (B2), $\mathcal{H}_1$ is the block diagonal part omitting the diagonal part of Eq. (B2), and $\mathcal{H}_2(t)$ is the block off-diagonal part of Eq. (B2), which for the case of the EDSR mechanism described translates as the QD levels $\mathcal{H}_0 = \sum_{s,l} \varepsilon_{1,l}^{K',s} |s,l\rangle \langle s,l|$, in-plane magnetic field Eq. (4) for $\mathcal{H}_1$, and ac-electric field matrix elements Eq. (6) for $\mathcal{H}_2$. Only

$S_1(t)$ needs to be solved for, which is done by applying the $\tilde{\mathcal{H}}(t)_{\text{off-diagonal}} = 0$ condition, giving

$$[\mathcal{H}_0, S(t)^{(1)}] = -\mathcal{H}_2. \tag{B7}$$

So finally, a block diagonal of the qubit and the excited orbital space may be approximated where the qubit space of Eq. (B5) is given as Eq. (10).

---

[1] Q. H. Wang, K. Kalantar-Zadeh, A. Kis, J. N. Coleman, and M. S. Strano, Nat. Nanotechnol. **7**, 699 (2012).

[2] A. Kumar and P. Ahluwalia, Eur. Phys. J. B **85**, 186 (2012).

[3] M. Chhowalla, H. S. Shin, G. Eda, L.-J. Li, K. P. Loh, and H. Zhang, Nat. Chem. **5**, 263 (2013).

[4] Y. Zhang, T.-R. Chang, B. Zhou, Y.-T. Cui, H. Yan, Z. Liu, F. Schmitt, J. Lee, R. Moore, Y. Chen *et al.*, Nat. Nanotechnol. **9**, 111 (2014).

[5] A. Kormányos, G. Burkard, M. Gmitra, J. Fabian, V. Zólyomi, N. D. Drummond, and V. Falko, 2D Mater. **2**, 022001 (2015).

[6] A. Splendiani, L. Sun, Y. Zhang, T. Li, J. Kim, C.-Y. Chim, G. Galli, and F. Wang, Nano Lett. **10**, 1271 (2010).

[7] K. F. Mak, C. Lee, J. Hone, J. Shan, and T. F. Heinz, Phys. Rev. Lett. **105**, 136805 (2010).

[8] D. Xiao, G.-B. Liu, W. Feng, X. Xu, and W. Yao, Phys. Rev. Lett. **108**, 196802 (2012).

[9] X. Xu, W. Yao, D. Xiao, and T. F. Heinz, Nat. Phys. **10**, 343 (2014).

[10] Z. Zhu, Y. Cheng, and U. Schwingenschlögl, Phys. Rev. B **84**, 153402 (2011).

[11] G. Wang, C. Robert, A. Suslu, B. Chen, S. Yang, S. Alamdari, I. C. Gerber, T. Amand, X. Marie, S. Tongay, and B. Urbaszek, Nat. Commun. **6**, 10110 (2015).

[12] D. Çakır, F. M. Peeters, and C. Sevik, Appl. Phys. Lett. **104**, 203110 (2014).

[13] C. Palacios-Berraquero, D. M. Kara, A. R.-P. Montblanch, M. Barbone, P. Latawiec, D. Yoon, A. K. Ott, M. Loncar, A. C. Ferrari, and M. Atatüre, Nat. Commun. **8**, 15093 (2017).

[14] A. K. Geim and I. V. Grigorieva, Nature (London) **499**, 419 (2013).

[15] F. Withers, O. Del Pozo-Zamudio, A. Mishchenko, A. Rooney, A. Gholinia, K. Watanabe, T. Taniguchi, S. Haigh, A. Geim, A. Tartakovskii, and K. S. Novoselov, Nat. Mater. **14**, 301 (2015).

[16] D. Zhong, K. L. Seyler, X. Linpeng, R. Cheng, N. Sivadas, B. Huang, E. Schmidgall, T. Taniguchi, K. Watanabe, M. A. McGuire *et al.*, Sci. Adv. **3**, e1603113 (2017).

[17] R. Pisoni, Z. Lei, P. Back, M. Eich, H. Overweg, Y. Lee, K. Watanabe, T. Taniguchi, T. Ihn, and K. Ensslin, Appl. Phys. Lett. **112**, 123101 (2018).

[18] A. Branny, S. Kumar, R. Proux, and B. D. Gerardot, Nat. Commun. **8**, 15053 (2017).

[19] J. Kern, I. Niehues, P. Tonndorf, R. Schmidt, D. Wigger, R. Schneider, T. Stiehm, S. Michaelis de Vasconcellos, D. E. Reiter, T. Kuhn, and R. Bratschitsch, Adv. Mater. **28**, 7101 (2016).

[20] J. Lin, O. Cretu, W. Zhou, K. Suenaga, D. Prasai, K. I. Bolotin, N. T. Cuong, M. Otani, S. Okada, A. R. Lupini *et al.*, Nat. Nanotechnol. **9**, 436 (2014).

[21] J. Klinovaja and D. Loss, Phys. Rev. B **88**, 075404 (2013).

[22] Z. Fei, T. Palomaki, S. Wu, W. Zhao, X. Cai, B. Sun, P. Nguyen, J. Finney, X. Xu, and D. H. Cobden, Nat. Phys. **13**, 677 (2017).

[23] Y. Ma, L. Kou, X. Li, Y. Dai, and T. Heine, Phys. Rev. B **93**, 035442 (2016).

[24] X. Xi, Z. Wang, W. Zhao, J.-H. Park, K. T. Law, H. Berger, L. Forró, J. Shan, and K. F. Mak, Nat. Phys. **12**, 139 (2016).

[25] Y.-T. Hsu, A. Vaezi, M. H. Fischer, and E.-A. Kim, Nat. Commun. **8**, 14985 (2017).

[26] A. F. Morpurgo, Nat. Phys. **9**, 532 (2013).

[27] T. S. Ghiasi, J. Ingla-Aynés, A. A. Kaverzin, and B. J. van Wees, Nano Lett. **17**, 7528 (2017).

[28] J. R. Schaibley, H. Yu, G. Clark, P. Rivera, J. S. Ross, K. L. Seyler, W. Yao, and X. Xu, Nat. Rev. Mater. **1**, 16055 (2016).

[29] Y. K. Luo, J. Xu, T. Zhu, G. Wu, E. J. McCormick, W. Zhan, M. R. Neupane, and R. K. Kawakami, Nano Lett. **17**, 3877 (2017).

[30] X. Yin, Z. Ye, D. A. Chenet, Y. Ye, K. OBrien, J. C. Hone, and X. Zhang, Science **344**, 488 (2014).

[31] H. Zeng and X. Cui, Chem. Soc. Rev. **44**, 2629 (2015).

[32] K. Kośmider, J. W. González, and J. Fernández-Rossier, Phys. Rev. B **88**, 245436 (2013).

[33] A. Kormányos, V. Zólyomi, N. D. Drummond, P. Rakyta, G. Burkard, and V. I. Fal'ko, Phys. Rev. B **88**, 045416 (2013).

[34] A. Srivastava, M. Sidler, A. V. Allain, D. S. Lembke, A. Kis, and A. Imamoğlu, Nat. Phys. **11**, 141 (2015).

[35] Z. Wang, J. Shan, and K. F. Mak, Nat. Nanotechnol. **12**, 144 (2017).

[36] R.-L. Chu, X. Li, S. Wu, Q. Niu, W. Yao, X. Xu, and C. Zhang, Phys. Rev. B **90**, 045427 (2014).

[37] T. Lyons, S. Dufferwiel, M. Brooks, F. Withers, T. Taniguchi, K. Watanabe, K. Novoselov, G. Burkard, and A. Tartakovskii, Nat. Commun. **10**, 2330 (2019).

[38] H. Yu, G.-B. Liu, P. Gong, X. Xu, and W. Yao, Nat. Commun. **5**, 3876 (2014).

[39] A. Kormányos, V. Zólyomi, V. I. Fal'ko, and G. Burkard, Phys. Rev. B **98**, 035408 (2018).

[40] J. Pawłowski, D. Żebrowski, and S. Bednarek, Phys. Rev. B **97**, 155412 (2018).

[41] J. Pawłowski, New J. Phys. **21**, 123029 (2019).

[42] M. Brotons-Gisbert, A. Branny, S. Kumar, R. Picard, R. Proux, M. Gray, K. S. Burch, K. Watanabe, T. Taniguchi, and B. D. Gerardot, Nat. Nanotechnol. **14**, 442 (2019).

[43] A. Kormányos, V. Zólyomi, N. D. Drummond, and G. Burkard, Phys. Rev. X **4**, 011034 (2014).

[44] G. Széchenyi, L. Chirolli, and A. Pályi, 2D Mater. **5**, 035004 (2018).

[45] A. David, G. Burkard, and A. Kormányos, 2D Mater. **5**, 035031 (2018).

[46] M. Brooks and G. Burkard, Phys. Rev. B **95**, 245411 (2017).

[47] C. Zhao, T. Norden, P. Zhang, P. Zhao, Y. Cheng, F. Sun, J. P. Parry, P. Taheri, J. Wang, Y. Yang *et al.*, Nat. Nanotechnol. **12**, 757 (2017).

[48] K. L. Seyler, D. Zhong, B. Huang, X. Linpeng, N. P. Wilson, T. Taniguchi, K. Watanabe, W. Yao, D. Xiao, M. A. McGuire *et al.*, Nano Lett. **18**, 3823 (2018).

[49] B. Huang, G. Clark, E. Navarro-Moratalla, D. R. Klein, R. Cheng, K. L. Seyler, D. Zhong, E. Schmidgall, M. A. McGuire, D. H. Cobden *et al.*, Nature **546**, 270 (2017).

[50] J. Qi, X. Li, Q. Niu, and J. Feng, Phys. Rev. B **92**, 121403(R) (2015).

[51] B. Scharf, G. Xu, A. Matos-Abiague, and I. Žutić, Phys. Rev. Lett. **119**, 127403 (2017).

[52] N. Cortés, O. Ávalos-Ovando, L. Rosales, P. A. Orellana, and S. E. Ulloa, Phys. Rev. Lett. **122**, 086401 (2019).

[53] Z. Wang, K. F. Mak, and J. Shan, Phys. Rev. Lett. **120**, 066402 (2018).

[54] M. Russ and G. Burkard, J. Phys.: Condens. Matter **29**, 393001 (2017).

[55] V. N. Golovach, M. Borhani, and D. Loss, Phys. Rev. B **74**, 165319 (2006).

[56] G.-H. Lee, X. Cui, Y. D. Kim, G. Arefe, X. Zhang, C.-H. Lee, F. Ye, K. Watanabe, T. Taniguchi, P. Kim, and J. Hone, ACS Nano **9**, 7019 (2015).

[57] J. Romhányi, G. Burkard, and A. Pályi, Phys. Rev. B **92**, 054422 (2015).

[58] Y. Zhou, G. Scuri, D. S. Wild, A. A. High, A. Dibos, L. A. Jauregui, C. Shu, K. De Greve, K. Pistunova, A. Y. Joe *et al.*, Nat. Nanotechnol. **12**, 856 (2017).

[59] F. Cadiz, E. Courtade, C. Robert, G. Wang, Y. Shen, H. Cai, T. Taniguchi, K. Watanabe, H. Carrere, D. Lagarde *et al.*, Phys. Rev. X **7**, 021026 (2017).

[60] G. Scuri, Y. Zhou, A. A. High, D. S. Wild, C. Shu, K. De Greve, L. A. Jauregui, T. Taniguchi, K. Watanabe, P. Kim *et al.*, Phys. Rev. Lett. **120**, 037402 (2018).

[61] K. Pistunova, L. Jauregui, A. Joe, K. De Greve, A. Sushko, D. Rhodes, J. Hone, H. Park, M. Lukin, and P. Kim, Bull. Am. Phys. Soc. **64**, A15.00007 (2019).

[62] T. Obata, M. Pioro-Ladrière, Y. Tokura, Y.-S. Shin, T. Kubo, K. Yoshida, T. Taniyama, and S. Tarucha, Phys. Rev. B **81**, 085317 (2010).

[63] S. Nadj-Perge, S. Frolov, E. Bakkers, and L. P. Kouwenhoven, Nature (London) **468**, 1084 (2010).

[64] E. Kawakami, P. Scarlino, D. R. Ward, F. Braakman, D. Savage, M. Lagally, M. Friesen, S. N. Coppersmith, M. A. Eriksson, and L. Vandersypen, Nat. Nanotechnol. **9**, 666 (2014).

[65] L. Yang, N. A. Sinitsyn, W. Chen, J. Yuan, J. Zhang, J. Lou, and S. A. Crooker, Nat. Phys. **11**, 830 (2015).